

Garnet Crystals

Discovery, Crystal Growth, and Characterization of Garnet
 $\text{Eu}_2\text{PbSb}_2\text{Zn}_3\text{O}_{12}$ Ryan Morrow,^{*,[a]} Mihai I. Sturza,^[a] Rajyavardhan Ray,^[a,b] Cameliu Himcinschi,^[c]
Jonas Kern,^[c] Philipp Schlender,^[d] Manuel Richter,^[a,b] Sabine Wurmehl,^[a] and
Bernd Büchner^[a,e]

Abstract: Single crystal specimens of previously unknown garnet $\text{Eu}_2\text{PbSb}_2\text{Zn}_3\text{O}_{12}$ were grown in a reactive $\text{PbO}:\text{PbF}_2$ flux medium. The crystals were characterized by a combination of X-ray crystallography, magnetization measurements, and the optical techniques of Raman, photoluminescence, and UV/Vis spectroscopy. The material exhibits Van Vleck paramagnetism associated with the $J = 0$ state of Eu^{3+} , which was possible to

accurately fit to a theoretical model. Band structure calculations were performed and compared to the experimental band gap of 1.98 eV. The crystals demonstrate photoluminescence associated with the $4f^6$ configuration of the Eu^{3+} ions sitting at the distorted 8-coordinate garnet A site. The title compound represents a unique quinary contribution to a relatively unexplored area of rare earth bearing garnet crystal chemistry.

Introduction

The garnet structure, a relatively common form of naturally occurring complex oxide, has the generalized formula of $\text{A}_3\text{B}_2\text{C}_3\text{O}_{12}$. The structure is composed of a network of corner sharing BO_6 octahedra and CO_4 tetrahedra, creating larger voids in which the A cations occupy a distorted 8-coordinate dodecahedral position.^[1] Beyond their aesthetic and geological significance, garnets have been the subject of broad disciplines of materials research. Some examples of these topics include lithium ion conductors,^[2,3] use as a lasing medium,^[4] and magneto-optical applications,^[5] as well as permanent,^[6] quantum,^[7] and frustrated magnets.^[8–11]

In this report, we present the synthesis, characterization and electronic properties of a previously unknown garnet $\text{Eu}_2\text{PbSb}_2\text{Zn}_3\text{O}_{12}$. Though related to an isolated report of $\text{Gd}_2\text{SrSb}_2\text{Zn}_3\text{O}_{12}$ and $\text{Gd}_2\text{CaSb}_2\text{Zn}_3\text{O}_{12}$,^[12] the title compound represents a unique quinary contribution to a relatively unexplored area of rare earth bearing garnet crystal chemistry. Using a combination of experimental techniques, viz. magnetization, photoluminescence, Raman, and UV/Vis diffuse reflectance spectroscopy, and density functional theory (DFT), we study the crystal structure, magnetism, spectroscopic properties, and electronic structure of the title compound. As the material hosts Eu^{3+} cations in the distorted garnet A site, we investigate the material for potential photoluminescence.

Results and Discussion

Following the flux growth, the crystals discovered were of appreciable size (1–2 mm) and well faceted. Their color was a deep red, and they were translucent. However, as the EDX measurements and subsequently described diffraction experiments revealed, the initial target material of $\text{Eu}_3\text{Sb}_3\text{Zn}_2\text{O}_{14}$ had reacted with the flux during the growth process, incorporating Pb and producing the well-known and quickly recognizable garnet structure with new approximate formula $\text{Eu}_2\text{PbSb}_2\text{Zn}_3\text{O}_{12}$. The oxygen content in the formula was assumed by charge balancing and comparison to common garnet stoichiometries. More, precisely, the stoichiometry of the mixed A site is $\text{Eu}_{2.20(6)}\text{Pb}_{0.80(3)}\text{Sb}_2\text{Zn}_3\text{O}_{12}$ from EDX. There is no indication of the inclusion of F in the crystals (see supporting Figure 3) from EDX.

Powder XRD was performed on crushed crystals of $\text{Eu}_2\text{PbSb}_2\text{Zn}_3\text{O}_{12}$ to confirm the purity of the phase. The single-phase material was validated by the excellent match between

[a] Dr. R. Morrow, Dr. M. I. Sturza, Dr. R. Ray, Dr. M. Richter, Dr. S. Wurmehl, Prof. Dr. B. Büchner

Leibniz Institute for Solid State and Materials Research Dresden IFW
Helmholtzstr. 20, D-01069 Dresden, Germany
E-mail: r.c.morrow@ifw-dresden.de

[b] Dr. R. Ray, Dr. M. Richter
Dresden Center for Computational Materials Science (DCMS),
Technische Universität Dresden,
D-01062 Dresden, Germany

[c] Dr. C. Himcinschi, J. Kern
Institute of Theoretical Physics, TU Bergakademie Freiberg,
D-09599, Freiberg, Germany

[d] Dr. P. Schlender
Faculty of Chemistry and Food Chemistry, Technische Universität Dresden,
D-01062 Dresden, Germany

[e] Prof. Dr. B. Büchner
Institut für Festkörperphysik, Technische Universität Dresden,
D-01069 Dresden, Germany

Supporting information and ORCID(s) from the author(s) for this article are available on the WWW under <https://doi.org/10.1002/ejic.202000271>.

© 2020 The Authors. Published by Wiley-VCH Verlag GmbH & Co. KGaA. This is an open access article under the terms of the Creative Commons Attribution License, which permits use, distribution and reproduction in any medium, provided the original work is properly cited.

the calculated and the experimental powder XRD patterns using Rietveld refinements. Figure 1 depicts the results of refinement, agreement factors, and refined lattice constants of powder XRD patterns (Cu- $K_{\alpha 1}$ radiation) of the sample studied in this work. The results are in good agreement (Bragg R-factor = 2.84, R_f -factor = 3.94) with the structure parameters determined by single crystal XRD.

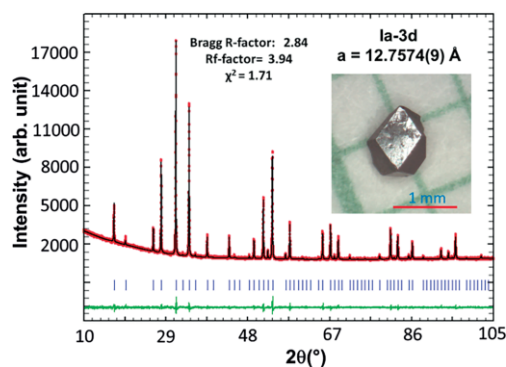


Figure 1. Calculated (black line), observed (red open circle) and difference (light green line) XRD patterns of the Rietveld refinement for $\text{Eu}_2\text{PbSb}_2\text{Zn}_3\text{O}_{12}$ ($\lambda = 1.5406 \text{ \AA}$, Bragg R-factor: 2.84 %; R_f -factor = 3.94 %). The inset depicts a typical crystal of $\text{Eu}_2\text{PbSb}_2\text{Zn}_3\text{O}_{12}$.

The single-crystal structures of the novel garnet $\text{Eu}_2\text{PbSb}_2\text{Zn}_3\text{O}_{12}$ were determined at room temperature (293 K) (Table 1, 2, 3, 4). The dark red polyhedral crystal crystallizes in the cubic space group $la-3d$, with cell parameters of $a = 12.7405(9) \text{ \AA}$ and $Z = 8$. The three dimensional (3D) structure of $\text{Eu}_2\text{PbSb}_2\text{Zn}_3\text{O}_{12}$ depicted in Figure 2(a) can be regarded as a typical example of the garnet structure. The general formula for garnet is $A_3B_2C_3O_{12}$, where A , B and C are cations at different symmetry sites. Garnets have a cubic crystal structure but with a complicated arrangement of different cations in the unit cell. The garnet structure can be explained in terms of a 160 atom body-centered cubic unit cell. For $\text{Eu}_2\text{PbSb}_2\text{Zn}_3\text{O}_{12}$ garnet: the 8-fold dodecahedral A site (24c – D2 point symmetry) is occupied by mixed 73.2(17)% Eu^{3+} and 26.8(17)% Pb^{2+} ; the 6-fold octahedral B site (16a – S6 point symmetry) is occupied by Sb^{5+} while the 4-fold tetrahedral C site (24d – S4 point symmetry) is occupied by Zn^{2+} . The refined occupation of the A site is in excellent agreement with the ratio determined by EDX (73.3 % Eu^{3+} and 26.7 % Pb^{2+}). The coordination environments of mixed Eu/Pb atoms are shown in Figure 2(b). The $\text{Eu}^{3+}/\text{Pb}^{2+}$ triangular dodecahedron is assembled by four $\text{Eu}/\text{Pb}-\text{O}$ bonds in the range of 2.440(3) \AA and another four in the range of 2.561(3) \AA . The Sb^{5+} octahedron depicted in Figure 2(c) is built up from six $\text{Sb}-\text{O}$ bonds which measures 1.987(3) \AA . The Zn^{2+} has four O^{2-} neighbors in a tetrahedral fashion, Figure 2(d), with four sets of $\text{Zn}-\text{O}$ bonds with a distance of 1.952(3) \AA . Each octahedron is connected to six tetrahedra while each tetrahedron is connected to four $[\text{SbO}_6]$ octahedra by sharing corners.

Deposition Number 1950530 (for $\text{Eu}_2\text{PbSb}_2\text{Zn}_3\text{O}_{12}$) contains the supplementary crystallographic data for this paper. These data are provided free of charge by the joint Cambridge Crystallographic Data Centre and Fachinformationszentrum Karlsruhe Access Structures service www.ccdc.cam.ac.uk/structures.

Table 1. Summary of crystallographic data and structure refinement for $\text{Eu}_2\text{PbSb}_2\text{Zn}_3\text{O}_{12}$ at 293K.

Empirical formula	$\text{Eu}_{2.196}\text{Pb}_{0.804}\text{Sb}_2\text{Zn}_3\text{O}_{12}$
Formula weight	1132.72
Wavelength	0.71073 \AA
Crystal system	cubic
Space group	$la-3d$
Unit cell dimension	$a = 12.7405(9) \text{ \AA}$
Volume	2068.0(4) \AA^3
Z	8
Density (calculated)	7.272 g/cm^3
Absorption coefficient	37.496 mm^{-1}
$F(000)$	3938
θ range for data collection	3.918 to 32.447 $^\circ$
Index ranges	$-19 \leq h \leq 19, -19 \leq k \leq 19, -19 \leq l \leq 19$
Reflections collected	39904
Independent reflections	316 [$R_{\text{int}} = 0.0829$]
Completeness to $\theta = 25.242^\circ$	99.4 %
Refinement method	Full-matrix least-squares on F^2
Data/restraints/parameters	316/ 0/ 19
Goodness-of-fit	1.473
Final R indices [$I > 2\sigma(I)$] ^[a]	$R_{\text{obs}} = 0.0243, wR_{\text{obs}} = 0.0651$
R indices [all data]	$R_{\text{all}} = 0.0246, wR_{\text{all}} = 0.0653$
Extinction coefficient	0.00138(9)

[a] $R = \frac{\sum ||F_o| - |F_c||}{\sum |F_o|}$, $wR = \frac{\{\sum [w(|F_o|^2 - |F_c|^2)]^2 / \sum [w(|F_o|^4)]\}^{1/2}}$ and $w = 1/[\sigma^2(F_o^2) + (0.0317P)^2 + 89.7942P]$ where $P = (F_o^2 + 2F_c^2)/3$.

Table 2. Atomic coordinates and equivalent isotropic displacement parameters ($\text{ \AA}^2 \times 10^3$) of $\text{Eu}_2\text{PbSb}_2\text{Zn}_3\text{O}_{12}$ at 293(2) K with estimated standard deviations in parentheses.

Label	Wyck	x	y	z	Occupancy	U_{eq} [a]
Eu	24c	1/8	0	1/4	0.732(17)	0.0060(2)
Pb	24c	1/8	0	1/4	0.268(17)	0.0060(2)
Sb	16a	0	0	0	1	0.0033(3)
Zn	24d	3/8	0	1/4	1	0.0066(3)
O	96 h	-0.1445(2)	0.265(3)	-0.517(3)	1	0.0096(6)

[a] U_{eq} is defined as one third of the trace of the orthogonalized U_{ij} tensor.

Table 3. Anisotropic displacement parameters (\AA^2) for $\text{Eu}_2\text{PbSb}_2\text{Zn}_3\text{O}_{12}$ at 293(2) K with estimated standard deviations in parentheses.

Label	U_{11}	U_{22}	U_{33}	U_{12}	U_{13}	U_{23}
Eu	0.0047(2)	0.0066(2)	0.0066(2)	0.00095(10)	0	0
Pb	0.0047(2)	0.0066(2)	0.0066(2)	0.00095(10)	0	0
Sb	0.0033(3)	0.0033(3)	0.0033(3)	-0.00032(9)	-0.00032(9)	-0.00032(9)
Zn	0.0049(5)	0.0074(4)	0.0074(4)	0	0	0
O	0.0053(13)	0.0104(14)	0.0131(15)	-0.0043(10)	-0.0009(10)	0.0038(10)

The anisotropic displacement factor exponent takes the form: $-2\pi^2[h^2a^2U_{11} + \dots + 2hka^*b^*U_{12}]$.

Table 4. Representative bond lengths (\AA) and bond angles ($^\circ$) of $\text{Eu}_2\text{PbSb}_2\text{Zn}_3\text{O}_{12}$ at 293(2) K.

atom-atom	bond lengths	atom-atom-atom	bond angle
$\text{Eu}/\text{Pb} - \text{O} (\times 4)$	2.440(3)	$\text{O} - \text{Eu}/\text{Pb} - \text{O}$	109.15(15)
$\text{Eu}/\text{Pb} - \text{O} (\times 4)$	2.561(3)	$\text{O} - \text{Eu}/\text{Pb} - \text{O}$	75.52(14)
$\text{Eu}/\text{Pb} - \text{Zn} (\times 2)$	3.1851(2)	$\text{O} - \text{Eu}/\text{Pb} - \text{Zn}$	157.20(15)
$\text{Eu}/\text{Pb} - \text{Sb} (\times 2)$	3.5611(3)	$\text{O} - \text{Eu}/\text{Pb} - \text{Zn}$	64.59(14)
$\text{Sb} - \text{O} (\times 6)$	1.987(3)	$\text{O} - \text{Sb} - \text{O}$	180.0
$\text{Zn} - \text{O} (\times 4)$	1.952(3)	$\text{O} - \text{Sb} - \text{O}$	95.42(13)
		$\text{O} - \text{Sb} - \text{O}$	84.58(13)
		$\text{O} - \text{Zn} - \text{O}$	114.46(11)
		$\text{O} - \text{Zn} - \text{O}$	99.9(2)

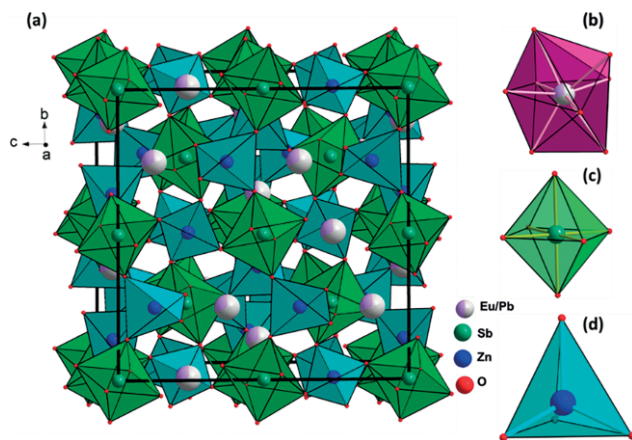


Figure 2. (a) Perspective view of the 3D structure of $\text{Eu}_2\text{PbSb}_2\text{Zn}_3\text{O}_{12}$ down the crystallographic a -axis. (b) $\text{Eu}^{3+}/\text{Pb}^{2+}$ dodecahedron (CN = 8); (c) Sb^{5+} octahedron (CN = 6) and (d) Zn^{2+} tetrahedron (CN = 4). Eu/Pb atoms are gray/lavender with refined occupation of 0.732(17):0.268(17), Sb atoms green, Zn atoms blue and O atoms red.

The temperature dependence of the magnetic susceptibility of $\text{Eu}_2\text{PbSb}_2\text{Zn}_3\text{O}_{12}$ is shown in Figure 3(a). Below ca. 100 K, an onset of temperature independent Van Vleck type paramagnetism is evident due to the Eu^{3+} ground state of 7F_0 ($S = 3$, $L = 3$). Such a gradual transition is commonplace in many materials incorporating Eu^{3+} cations,^[13,26] including related garnet material $\text{Eu}_3\text{Ga}_5\text{O}_{12}$.^[27] In the lowest temperature range, a Curie tail is evidence of the presence of some concentration of paramagnetic defects or impurity phases, a common occurrence. Therefore, we model the magnetic susceptibility of the garnet compound as:

$$\chi_{\text{tot}} = (1 - p)\chi_{\text{VV}} + p\chi_{\text{Imp}} \quad (1)$$

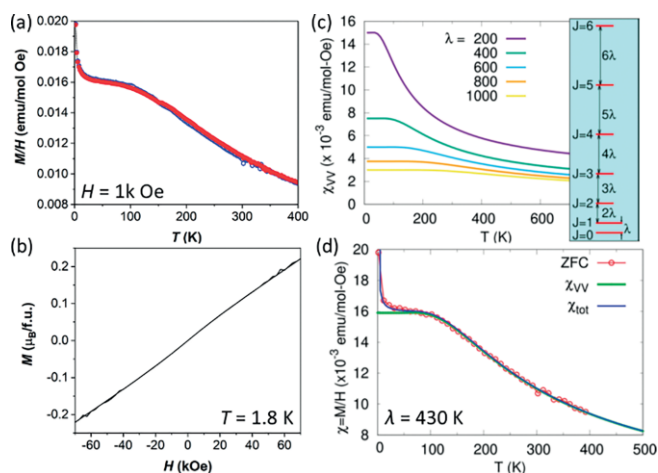


Figure 3. (a) Temperature dependence of the magnetic susceptibility of $\text{Eu}_2\text{PbSb}_2\text{Zn}_3\text{O}_{12}$ measured under an applied field of 1 kOe and zero field cooled (blue) and field cooled conditions (red). The curves approximately overlap. (b) Field dependence of the magnetization of $\text{Eu}_2\text{PbSb}_2\text{Zn}_3\text{O}_{12}$ measured at 1.8 K. (c) The Van Vleck paramagnetic susceptibility for Eu^{3+} ions as a function of temperature for different values of on-site spin orbit coupling λ [K]. The inset shows the relative splitting of the multiplets 7F_J which depend only on λ . (d) The fit of the zero field cooled (ZFC) data considering only Van Vleck paramagnetism (χ_{VV}) and the full model considering also additional contribution from the Eu^{2+} impurity ions (χ_{imp}). The fitting parameters are shown in Table 5.

where p is the concentration of the presumed Eu^{2+} impurity ions. χ_{VV} and χ_{Imp} , respectively, represent the contribution of the Van Vleck paramagnetism (from Eu^{3+} ions) and the Eu^{2+} impurity ions. The Van Vleck paramagnetic susceptibility is obtained by considering the spin-orbit splitting of the lowest multiplet 7F_J of the Eu^{3+} ions (see the inset of Figure 3(c)). The splitting of the energy levels depends only on the spin-orbit coupling parameter λ and χ_{VV} can be modeled as:^[26,28]

$$\chi_{\text{VV}} = \frac{N\mu_B^2}{\lambda} \left(\frac{A}{Z} \right), \quad (2a)$$

$$Z = 1 + 3e^{-\lambda/k_B T} + 5e^{-3\lambda/k_B T} + 7e^{-6\lambda/k_B T} + 9e^{-10\lambda/k_B T} + 11e^{-15\lambda/k_B T} + 13e^{-21\lambda/k_B T}, \quad (2b)$$

$$A = 8 + \left(\frac{9\lambda}{2k_B T} - \frac{1}{2} \right) e^{-\lambda/k_B T} + \left(\frac{45\lambda}{2k_B T} - \frac{5}{6} \right) e^{-3\lambda/k_B T} + \left(\frac{63\lambda}{k_B T} - \frac{7}{6} \right) e^{-6\lambda/k_B T} + \left(\frac{135\lambda}{k_B T} - \frac{3}{2} \right) e^{-10\lambda/k_B T} + \left(\frac{495\lambda}{2k_B T} - \frac{11}{6} \right) e^{-15\lambda/k_B T} + \left(\frac{819\lambda}{2k_B T} - \frac{13}{6} \right) e^{-21\lambda/k_B T}. \quad (2c)$$

N is the number of Eu ions and Z is the partition function. Figure 3(c) shows the dependence of the Van Vleck paramagnetism on λ . For any value of λ , there is a temperature independent part (plateau) at low temperatures. With increasing values of λ , there are two characteristic features: (i) the onset of the plateau shifts to higher temperatures, and (ii) the magnitude of the temperature independent susceptibility decreases. These λ -dependent characteristics are simply due to manifestation of the fact that the contribution of the excited states to the magnetic susceptibility decreases with increasing λ .

As these equations involve only one free parameter λ , its value can, in principle, be obtained by comparing the calculated Van Vleck susceptibility and the corresponding experimental data. However, for the garnet system under consideration, since the Eu^{3+} ions share the Wyckoff position with non-magnetic Pb atoms as well as with Eu^{2+} impurities, we consider N as another free parameter. Later, to cross-check our model, we compare the value of N obtained from fitting the magnetic susceptibility data with the value estimated from the XRD refinement. For brevity, we relabel the prefactor in Eq. (2a) as $\alpha = N\mu_B^2$. For molar susceptibility, we use $\alpha_0 = (N_A/\text{mol})\mu_B^2 = 0.34512 \text{ emu}\cdot\text{K}/\text{mol}\cdot\text{Oe}$ as reference, where N_A is the Avogadro number, equal to number of free ions in one mol.

The magnetic susceptibility of Eu^{2+} impurity ions is modeled as:^[29]

$$\chi_{\text{Imp}} = \frac{C}{T}, \quad (3)$$

where $C = 7.875 \text{ emu}/\text{mol}$ is the Curie constant of Eu^{2+} ions,^[30] leading to three free parameters in the full model represented by Eq. (1): λ , α , and p . Figure 3(d) shows the fit of χ_{VV} , which accounts for only the Van Vleck paramagnetic susceptibility represented by Eq. (2) and, the full model χ_{tot} (Eq. (1)), which accounts also for the contributions of the impurity ions to the experimental data. The fitting parameters are provided in Table 5. The value of spin-orbit coupling λ ca. 430 K is somewhat smaller than the 545.3 K for the free Eu^{3+} ions, but comparable to the values for Eu_2O_3 and other Van Vleck paramagnets containing Eu^{3+} ions.^[28]

The values of α obtained for both models are also comparable. Considering the model with only Eu^{3+} ions and Van Vleck paramagnetic susceptibility (Eq. (2)), the ratio of parameters $\alpha_{\text{VV}}/\alpha_0 = 2.24$ which suggests that the number of Eu atoms in the garnet system is ca. 2.2 times larger than in one mol of the free ions (Table 5). This value is in a very good agreement with the fraction of Eu ions estimated from the XRD data, whereby this fraction is estimated to be ca. 2.2, thus establishing that the considered model is indeed a good description of the observed magnetism. Within the full model, described by Eq. (1), the value of α is only slightly larger, still in a very good agreement. The fraction of Eu^{2+} impurities is found to be reasonably small, p ca. 0.1 %.

Considering the space group $la-3d$ (No. 230) and the occupancy of the Wyckoff positions as explained in the XRD section, the group theory predicts 3 A_{1g} , 8 doubly degenerated E_g and 14 triply degenerated T_{2g} Raman active modes.^[31,32] According to the polarisation selection rules for backscattering, the A_{1g} modes can be detected only in parallel configuration, while the E_g and the T_{2g} modes can be detected in both parallel and cross polarisation configurations.

The Raman and photoluminescence (PL) signals can be readily distinguished in the measured spectra by performing measurements with different excitation laser lines. In Figure 4 the spectra measured with 442 nm and 532 nm excitation wavelengths are shown for comparison. In the left side of the figure the Raman spectra are shown for both excitations. In the right hand of Figure 4 the PL signal (above 1000 cm^{-1}) detected at 532 nm excitation is shown. No luminescence was observed for 442 nm excitation in the measured range. For getting the absolute values of the PL peak positions in the 532 nm spectrum, the wavelength scale was also added on the top of the figure. The assignment of the Raman mode symmetry for a different garnet crystal belonging to the same space group $la-3d$ (No. 230) was done in literature based on Raman measurements performed on different crystal faces.^[33–36]

In Figure 5 the Raman spectra measured in backscattering geometry for parallel (VV) and cross (HV) polarisation configurations using 442 nm excitation for a (110) surface are shown. The spectra recorded at an azimuthal 90° rotation of the sample are also presented. The spectra exhibit an orientation dependence and a strong polarisation dependence of the intensity due to the Raman selection rules, with 18 Raman peaks identified in the $90\text{--}950\text{ cm}^{-1}$ range. (marked by * in Figure 5). However, a straightforward assignment of the phonon symmetry is still difficult because of the mixed Eu/Pb coordination. Based on the assignment of the Raman phonon modes for europium gallium garnet crystals^[37–39] the intensive peaks at 728 cm^{-1} and 516 cm^{-1} have A_{1g} symmetry. However, for these 2 intensive

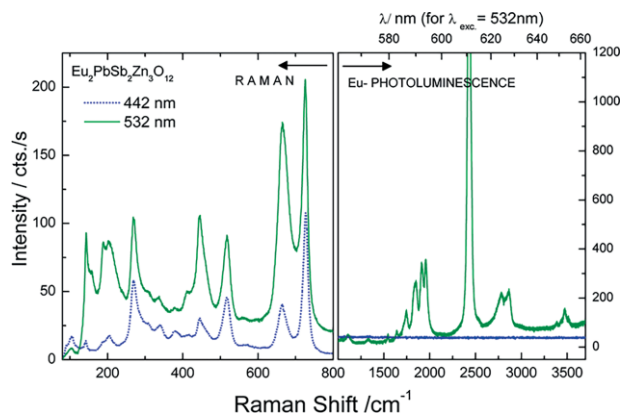


Figure 4. Raman (left side) and photoluminescence (right side) spectra measured on $\text{Eu}_2\text{PbSb}_2\text{Zn}_3\text{O}_{12}$ crystal using 442 nm (blue, dotted lower curves) and 532 nm (green, solid upper curves) excitations.

peaks ca. 5 % of the intensity could be still measured in the “forbidden” cross polarisation configuration due to polarisation leakages (due to the microscope objective) and/or sample misorientation. The third A_{1g} phonon can be the one at 271 cm^{-1} considering its nearly vanishing intensity in cross polarisation configuration. Its frequency is much lower than in $\text{Eu}_3\text{Ga}_5\text{O}_{12}$ (ca 340 cm^{-1})^[36,37,39] because of the involvement in the vibration of the heavier Pb atom.

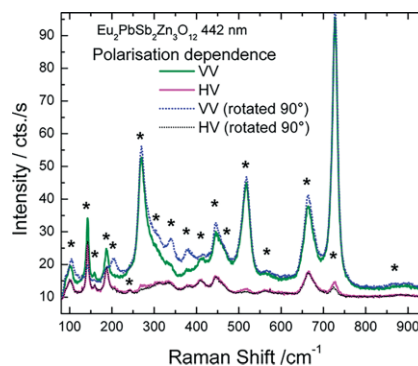


Figure 5. The Raman spectra of $\text{Eu}_2\text{PbSb}_2\text{Zn}_3\text{O}_{12}$ crystal measured in backscattering geometry for parallel (VV) and cross (HV) polarisation configurations. The spectra with azimuthal rotation of the sample by 90° are also shown.

In order to check the assignment of the modes, azimuthal dependent Raman measurements were performed. For this purpose, Raman spectra were measured by rotating the sample around the laser direction in steps of 15° for the azimuthal angle φ . A (110) surface of the crystal was measured for both parallel (VV) and cross (HV) polarization configurations. The intensity of the measured modes was analyzed by fitting the

Table 5. Fitting parameters.

Parameter	Van Vleck Paramagnetism (Eq. (2))	Full Model (Eq. (1), (2) and (3))
λ [K]	415.3 +/- 3.4	431.5 +/- 1.0
α (emu K/mol Oe)	0.8412 +/- 0.0052	0.8558 +/- 0.0014
p	–	0.000979 +/- 1.8E-05
r.m.s of residuals	3.44658 E-04	8.78208 E-05
Variance of residuals	1.18789 E-07	7.71249 E-09

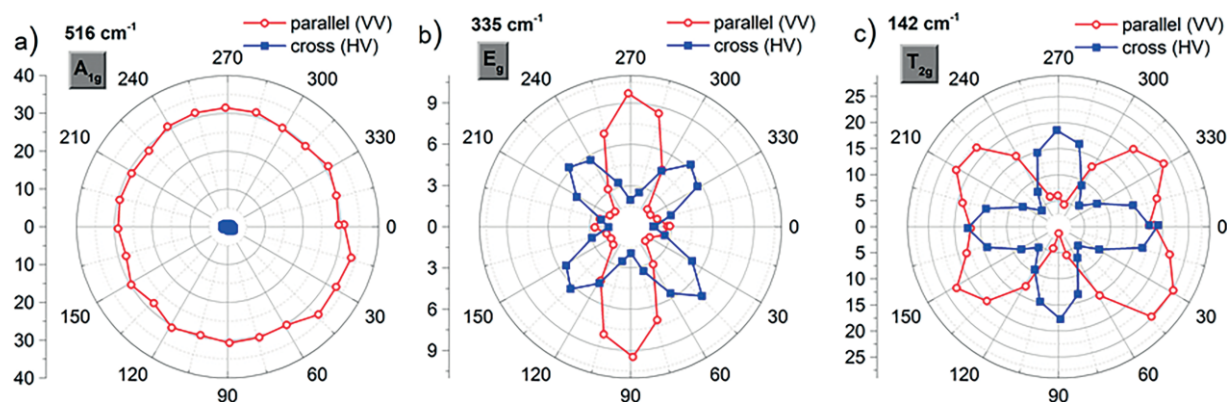


Figure 6. Polar plots of the azimuthal angle (φ) dependence of the intensity for the modes at 516 cm^{-1} (a), 335 cm^{-1} (b), and 142 cm^{-1} (c) having A_{1g} , E_g , and T_{2g} symmetries, respectively.

peaks by Lorentzian oscillators for each angle and polarization configuration. The angular dependence of the intensity was used for the assignment of the modes, by using the Raman tensor formalism in a procedure similar to the one we introduced for BiFeO_3 crystals.^[40]

By using polar plots of intensity vs. azimuthal angle (φ), the A_{1g} modes could be easily identified because of their nearly constant intensity in parallel polarization configuration and vanishing intensity for cross polarization configuration. Figure 6(a) shows exemplary the polar plot of the A_{1g} mode at 516 cm^{-1} . Very similar behavior was found for the other two A_{1g} modes at 271 cm^{-1} and 728 cm^{-1} . The expected dependences of the intensity on azimuthal angle (φ) for all the modes, both polarizations and for the (110) scattering surface are given in Table 6.

Table 6. The expected azimuthal angle (φ) dependence of the intensity of the A_{1g} , E_g , and T_{2g} modes for (110) scattering surface, for parallel (p) and cross (c) polarization configurations obtained using the Raman tensor formalism.^[40] a, b, and d are connected to the Raman tensor elements of the A_{1g} , E_g , and T_{2g} modes respectively.^[32,33]

Intensity	(110) scattering
$I_p^{A_{1g}} \sim$	a^2
$I_c^{A_{1g}} \sim$	0
$I_p^{E_g} \sim$	$b^2(4 - 3(\cos^4(\varphi) + \sin^2(2\varphi)))$
$I_c^{E_g} \sim$	$\frac{9}{4}b^2\sin^2(2\varphi)$
$I_p^{T_{2g}} \sim$	$d^2(\cos^4(\varphi) + \sin^2(2\varphi))$
$I_c^{T_{2g}} \sim$	$d^2\left(\cos^2(2\varphi) + \frac{1}{4}\sin^2(2\varphi)\right)$

In the case of the E_g and T_{2g} modes the azimuthal dependence of the intensity is more complex, showing 180° periodicity for parallel polarization or 90° periodicity for cross polarization. At the angles where the intensity for parallel polarization shows

a maximum, there is a minimum in cross polarization and vice versa. In Figure 6(b) the polar plot for the E_g mode at 335 cm^{-1} is shown. Similar behavior has been observed for the modes at: ca. 101 cm^{-1} , 203 cm^{-1} , 279 cm^{-1} , 303 cm^{-1} , 382 cm^{-1} , 451 cm^{-1} , and 665 cm^{-1} , which indicate that these modes have an E_g symmetry. The experimental intensity dependence of the E_g modes is in good agreement with the dependence of the intensity predicted by the formulas in Table 6. In the Figure 6(c) the intensity dependence of the mode at 142 cm^{-1} , which has T_{2g} symmetry, is exemplary shown. The experimental intensity dependence is similar to the one expected from the formulas in Table 6 for the T_{2g} modes. The same dependence of the intensity shows also the modes at ca. 158 cm^{-1} , 187 cm^{-1} , 241 cm^{-1} and 410 cm^{-1} , which should have T_{2g} symmetry. In Table 7 the frequency positions and the symmetry assignment of the Raman modes are summarised.

Table 7. Assignment of the Raman modes of $\text{Eu}_2\text{PbSb}_2\text{Zn}_3\text{O}_{12}$.

Symmetry	Frequency/ cm^{-1}
A_{1g}	271, 516, 728
E_g	101, 203, 279, 303, 335, 382, 451, 665
T_{2g}	142, 158, 187, 241, 410

The most intensive peak observed in the PL spectrum at ca. 611 nm (Figure 4, right side) can be related to the Eu^{3+} transition from the excited state 5D_0 to 7F_2 .^[39,41] On the other hand the PL peaks in the $589\text{--}594\text{ nm}$ range were assigned to $^5D_0 \rightarrow ^7F_1$ transitions, while the other peaks correspond to different $D \rightarrow F$ multiplet transitions.^[41,42] Pressure dependent measurements of the PL intensities for the $^5D_0 \rightarrow ^7F_2$ and $^5D_0 \rightarrow ^7F_1$ transitions in Eu garnets and other Eu compounds suggest that an increase of the intensity of the $^5D_0 \rightarrow ^7F_2$ transition is related to an increase of the asymmetry around the Eu^{3+} ions.^[39,41,43,44] The high intensity measured at 611 nm in our PL spectra can, in this case, be correlated to a high asymmetry around the Eu^{3+} ions, which can also contribute to the difficulties in the assignment of some of the Raman phonons due to a partial relaxation of the selection rules.

To clarify the electronic properties, we start with UV/Vis diffuse reflectance spectroscopy to estimate the band gap. Furthermore, density functional theory (DFT) electronic structure

calculations were carried out. Due to random occupation of the Wyckoff sites 24c by Eu/Pb atoms, several inequivalent crystal structures were considered for DFT calculations to rule out any subtle occupation dependence. Specifically, nine distinct crystal structures (labelled S1–S9) corresponding to the 2:1 occupation of the Wyckoff sites 24c by Eu and Pb atoms, respectively, were considered (see “Computational Details”). Within the scalar relativistic calculations, the ground states for all the considered structures are semiconducting, with direct band gaps ranging between approximately 1.3 eV and 1.8 eV (see Table 8). Spin-orbit coupling has practically no effect on either the nature or the values of the band gap. These values are somewhat smaller than the corresponding experimental value of 1.98 eV, as obtained from the UV/Vis diffuse reflectance spectra, shown in Figure 7.

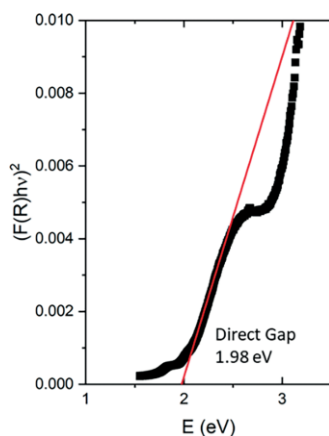


Figure 7. Kubelka–Munk transformation and linear extrapolation of UV/Vis diffuse reflectance data for the estimation of a direct band gap in $\text{Eu}_2\text{PbSb}_2\text{Zn}_3\text{O}_{12}$.

To further ascertain the robustness of the obtained nature of electronic band gap, the role of atomic positions was also investigated. The internal parameters (atomic positions) were optimized for the structures S3–S8 while keeping the lattice constants and angles fixed to their experimental values. While this influences the electronic band gap values significantly, the nature of the band gap remains unaffected. The band gaps for the relaxed structures lie between approximately 1.7 eV and 2.2 eV (see Table 8), in remarkably good agreement with the experimental value of 1.98 eV.

The qualitative features of the electronic structure are similar for all the considered structures. For a detailed discussion, we consider the structure “S7” as a representative. Within GGA, the ground state corresponds to a semiconductor with a direct band gap of ca. 1.83 eV. Inclusion of SOC merely lowers this gap by ca. 0.005 eV (see Table 8). However, the relaxed structure has a larger gap value of ca. 1.92 eV. Nevertheless, the nature of the electronic gap and qualitative aspects of the electronic structure remain unaffected. Figure 8(a) and (b) show the fully relativistic (with SOC) electronic band structure and the density of states (DOS) for “S7” with optimized atomic positions, clearly showing a direct band gap at the Γ point. The states above the Fermi energy (conduction band edge) are dominated by Sb and O contributions while the valence band edge is composed of

Table 8. Electronic band gaps of various $\text{Eu}_2\text{PbSb}_2\text{Zn}_3\text{O}_{12}$ structures considered in this study.

Case	Gap [eV]		
	Scalar Relativistic	Full Relativistic	Relaxed Structures (Full Relativistic)
S1	1.438	1.432	
S2	1.603	1.597	
S3	1.519	1.512	1.868
S4	1.330	1.323	1.731
S5	1.786	1.779	2.192
S6	1.487	1.481	1.827
S7	1.833	1.825	1.921
S8	1.518	1.508	2.091
S9	1.462	1.455	

Pb-6s and O-2p contributions from the nearest and next-nearest neighbor O atoms forming the PbO_8 dodecahedron, as shown in atom- and orbital-resolved DOS (see Figure 8(d) and (e)). The p-orbitals from these oxygen atoms strongly hybridize with Pb-6s orbitals and remain well-separated from the O-p dominated states in the valence band below ca. -1 eV. A small contribution from the more distant O atoms (O_3 atoms) in the energy range between -1 eV and the Fermi energy is also present. The unoccupied Pb-6p states imply a formal valency of +2 for Pb. This, in conjugation with the +3 valency of Eu atoms, implies that Sb and Zn are, respectively, in +5 and +2 states, in conformity with expectations.

The enhancement of the band gap upon optimization is accompanied and likely caused by the adjustment of oxygen atoms. For S7, the optimal Sb–O and Zn–O bond lengths are 2.021 Å and 1.943 Å, as compared to the experimental values of 1.987 Å and 1.952 Å (see Table 4). On the other hand, for Eu–O and Pb–O, while XRD suggests two distinct bond lengths forming the dodecahedron ($d_{\text{Eu/Pb-O1}} = 2.440$ Å and $d_{\text{Eu/Pb-O2}} = 2.561$ Å, also see Figure 2), in the lower symmetry model structures, dodecahedrons are twisted. More importantly, the size of the dodecahedrons depends on the central atom. Consequently, a distribution of bond lengths is realized with $\langle d_{\text{Eu-O}} \rangle = 2.456$ Å and $\langle d_{\text{Pb-O}} \rangle = 2.566$ Å (see Supplemental Material for details). In fact, these features are realized for all the considered structures, as shown in the Supplemental Material. Such local structural aspects can possibly be resolved by techniques more sensitive to oxygen positions, such as a neutron total scattering experiments and/or X-ray absorption fine structure (XAFS) spectroscopy, which, however, are beyond the scope of the present work.

Conclusion

Through a reaction with the crystal growth flux medium, dark red transparent single crystals of novel garnet $\text{Eu}_2\text{PbSb}_2\text{Zn}_3\text{O}_{12}$ were formed. Characterization methods of XRD and SQUID magnetometry as well as Raman, photoluminescence, and UV/Vis spectroscopy were performed and compared to theoretical methods. By Pb doping, a structure containing Eu^{3+} ions was realized which has properties of photoluminescence and Van Vleck paramagnetism. The new compound has potential applications associated with its wide band gap, intriguing pho-

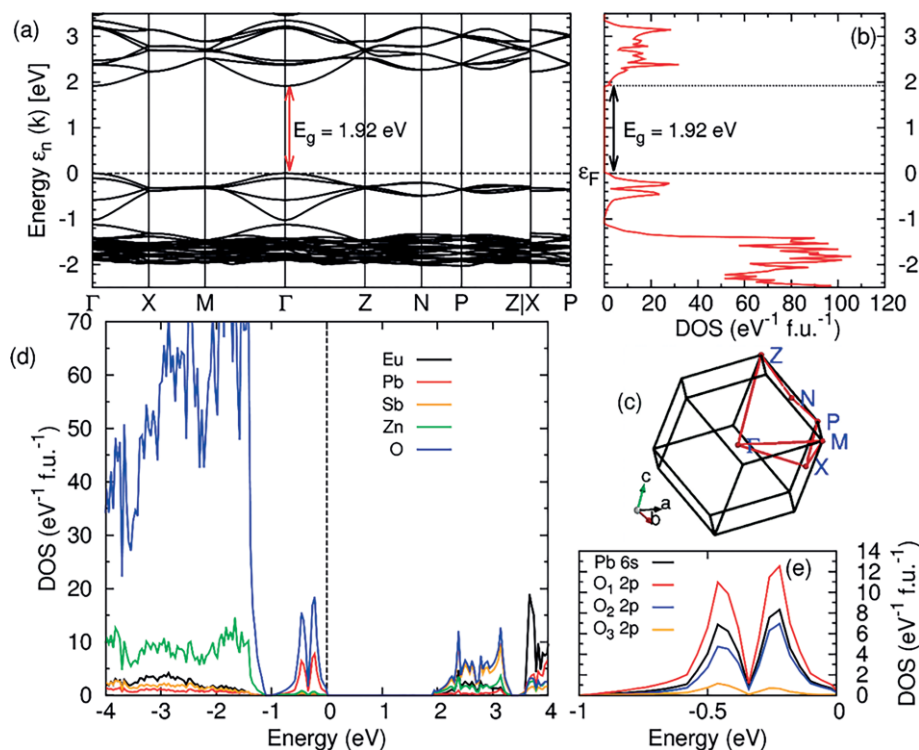


Figure 8. Electronic properties of $\text{Eu}_2\text{PbSb}_2\text{Zn}_3\text{O}_{12}$ garnet: (a) The band structure and (b) the total density of states per formula unit (f.u.) for the structure S7 with relaxed atomic positions. The high symmetry points in the Brillouin zone are shown in (c). (d) The atom-resolved DOS showing the relative contributions across the Fermi energy, and (e) zoom-in near the valence band edge showing that these bands are composed largely of Pb-6s and 2p states from O_1 and O_2 which form the dodecahedron shown in Figure 2(b). The other oxygen atoms O_3 are the third nearest neighbors.

oluminescent optical properties, and structural stability associated with the garnet structure.

Experimental Section

A 5 g sample of $\text{Eu}_3\text{Sb}_3\text{Zn}_2\text{O}_{14}$ was prepared by the direct solid state reaction of the dried binary oxides Eu_2O_3 , Sb_2O_5 , and ZnO at 1200 °C following the previous work of Sanders et al.^[13] 10 g of each PbO and PbF_2 were added to this to act as flux medium, and the mixture was placed in a Pt crucible with a Pt lid firmly crimped onto the top to limit the evaporation of the flux. This crucible was placed in a protective alumina casing and inserted into a muffle furnace located within a fumehood for safety due to the toxicity of the flux. The furnace was heated to 1200 °C, held for 24 hours, and slowly cooled to a rate of 1.7 °C per hour to a temperature of 600 °C before switching off the furnace. Afterwards, by tapping the bottom of the crucible with a rubber mallet, the soft flux was easily dislodged from the crucible and individual crystals could be directly removed and washed briefly in a dilute nitric acid bath. The chemical composition of the harvested crystals was examined by scanning electron microscopy (SEM, XL30 Philipps, IN400) equipped with an electron microprobe analyzer for semi-quantitative elemental analysis using the energy dispersive X-ray (EDX) mode, revealing the incorporation of lead into the formula $\text{Eu}_2\text{PbSb}_2\text{Zn}_3\text{O}_{12}$. Attempts to synthesize this new material in polycrystalline form through direct solid state synthesis of the pertinent binary oxides in a wide temperature range were unsuccessful, favoring the formation of pyrochlore related phases with no indication of the title garnet compound appearing in any quantity.

Crystals of $\text{Eu}_2\text{PbSb}_2\text{Zn}_3\text{O}_{12}$ were selected and mounted on the tips of glass fibers to perform single-crystal X-ray diffraction (XRD) experiments. Room-temperature intensity data were collected on a Bruker X8 Apex2 CCD4K using graphite-monochromatized Mo-K_α radiation ($\lambda = 0.71073 \text{ \AA}$). Data were collected over a full sphere of reciprocal space with 0.5° scans in ω with an exposure time of 15 s per frame. The 2θ range extended from 8° to 80° . The intensities were collected using φ and ω scans and extracted using the software package SAINT.^[14] Intensities were corrected from absorption effects using a semi-empirical method based on redundancy by use of the SADABS software.^[15] The crystal structure was refined using the SHELXL^[16] and JANA2006^[17] software packages. The crystal structure was solved by direct methods and refined by full-matrix least-squares on F^2 . The parameters for data collection and the details of the structure refinement are given in Table 1. Atomic coordinates, thermal displacement parameters (U_{eq}) and occupancies of all atoms are given in Table 2. Anisotropic displacement parameters and selected bond lengths and angles are given in Table 3 and Table 4.

Phase purity of the $\text{Eu}_2\text{PbSb}_2\text{Zn}_3\text{O}_{12}$ phase was confirmed by powder X-ray diffraction (XRD). The samples were finely ground and mounted on a thin film transmission sample holder to be analyzed with STOE STADI diffractometer in transmission geometry with Cu-K_α radiation equipped with a Germanium monochromator and a DECTRIS MYTHEN 1 K detector. Powder XRD data were analyzed with the Rietveld method using the FULLPROF SUITE program.^[18] The peak shape was assumed to be a pseudo-Voigt function and the refinement included the following features: (a) the background, which was extrapolated from 30 background parameters; (b) the scale factors; (c) the global instrumental parameters (zero-point 2θ

shift and systematic shifts, determined by transparency and off-centering of the sample); (d) the lattice parameter; and (e) the profile parameters (Caglioti half-width parameters of the pseudo-Voigt function). The March-Dollase model^[19] for preferred orientation was used in all of the refinements as the powders were prepared from crushed crystal specimens.

Magnetic property measurements were conducted on a Quantum Design SQUID Magnetic Property Measurement System (MPMS). A collection of randomly oriented crystals, totaling 35.0 mg were contained in a gel capsule and mounted in a straw for insertion into the device. The temperature dependence of the magnetization was measured under an applied field of 1 kOe following 1 kOe field cooled (FC) and zero field cooled (ZFC) conditions within the temperature range of 1.8 to 400 K. This procedure was repeated with a field of 50 kOe. The field dependence of the magnetization of the sample was measured within the range of -70 to +70 kOe at a temperature of 1.8 K. No corrections for diamagnetic contributions to the data were applied.

The diffuse reflectance spectra in the ultraviolet-visible (UV/Vis) range were collected using a Varian Cary 4000 UV/Vis spectrophotometer equipped with a Praying Mantis diffuse reflectance accessory (Harrick Scientific Products) between 200 and 800 nm. These measurements were conducted on powder from ground crystals. The data were transformed to an equivalent Kubelka-Munk absorption spectra $F(R)$ to estimate the direct band gap,^[20–22] which is obtained by plotting $[F(R)h\nu]^2$ as a function of energy $h\nu$. The intercept of the linear part of the spectrum near the absorption edge on the energy axis is equal to the optical band gap.^[22]

Micro Raman spectroscopy measurements were performed at room temperature using Horiba Jobin Yvon spectrometers equipped with 2400 mm^{-1} and 1800 mm^{-1} gratings. The excitation was done by means of 442 nm (HeCd laser) and 532 nm (frequency doubled Nd-YAG laser) lines, with a laser power below 1.5 mW. Backscattering geometry was employed with the laser propagation direction normal to the sample surface, and the incident and detected scattering polarisations being parallel (VV) or perpendicular (HV) to each other. A 50 \times magnification microscope objective was used and the spectra were recorded 20 times with an accumulation time of 5 s.

Computational Details

Considering the disordered occupation of the Wyckoff position 24c by Eu/Pb atoms, several different possible crystal structures for the $\text{Eu}_2\text{PbSb}_2\text{Zn}_3\text{O}_{12}$ compound were generated such that these (24c) sites are occupied by Eu and Pb atoms in the ratio 2:1. Our starting point was the hypothetical undoped $\text{Eu}_3\text{Sb}_2\text{Zn}_3\text{O}_{12}$ structure in the *Ia-3d* space group (see Table 2), which contains 12 Eu atoms per unit cell whose positions are related by symmetry operations corresponding to the Wyckoff position. Out of these, four atoms were randomly chosen using a pseudo random number generator and were replaced by Pb. In order to rule out any subtle dependence on the Pb-occupied sites, this procedure was carried out for approximately 30 different sets of sites (see Supplemental Material for details). In this way, nine distinct crystal structures were realized for which the electronic properties were investigated. While the list of obtained lower symmetry structures is not exhaustive, these structures are expected to form a representative sample.

All calculations were performed using the Perdew–Burke–Ernzerhof implementation^[23] of the Generalized Gradient Approximation (GGA) as implemented in the Full-Potential Local-Orbital (FPLO) code,^[24] version 18.52.^[25] A fine *k*-mesh with 8 \times 8 \times 8 intervals was used for numerical integration in the Brillouin zone along with a

linear tetrahedron method. Spin-orbit interactions (SOI) were included in the self-consistent calculations via the 4-spinor formalism as implemented in the FPLO code. For several structures, the internal coordinates (atomic positions) were optimized using the default scalar relativistic approximation implemented in the FPLO code and a coarser *k*-mesh with 2 \times 2 \times 2 intervals. The threshold for the residual forces on each atom during the optimization of internal coordinates was set to 1 meV/Å. The difference in the relaxed atomic position between the fine and the coarser *k*-meshes was found to be less than $10^{-3}a$ with *a* = lattice constant and the corresponding energy difference was $< 10^{-5}$ eV. Consequently, the resulting electronic properties were qualitatively the same.

In all cases, the Eu-4*f* orbitals were treated within the “open-core approximation”, where they are treated as core orbitals (no participation in bonding) despite partial occupations. Consistent with the low-temperature magnetic susceptibility measurements showing Van Vleck paramagnetism, non-magnetic 4*f*⁶ configuration corresponding to the *J* = 0 ground state multiplet was considered.

Acknowledgments

This work has been partially supported by the Deutsche Forschungsgemeinschaft through project B01 of SFB1143 (project ID 247310070). This work also is partially supported by the Deutsche Forschungsgemeinschaft through Grant STU 695/1-1 (M.S.). R.M. acknowledges support from the Alexander von Humboldt Foundation. R.R. and M.R. acknowledge financial support from the European Union (ERDF) and the Free State of Saxony via the ESF projects 100231947 and 100339533 (Young Investigators Group Computer Simulations for Materials Design – CoSiMa) during part of the project. The authors also gratefully acknowledge S. Gaß, S. Müller-Litvanyi, and U. Nitzsche for technical assistance. Open access funding enabled and organized by Projekt DEAL.

Keywords: Crystal growth · Solid State Chemistry · Magnetic properties · Garnet · Photoluminescence

- [1] A. F. Wells, *Structural Inorganic Chemistry*; Oxford, 1975.
- [2] R. Murugan, V. Thangadurai, W. Weppner, *Angew. Chem. Int. Ed.* **2007**, *46*, 7778–7781; *Angew. Chem.* **2007**, *119*, 7925https://doi.org/10.1002/anie.200701144.
- [3] V. Thangadurai, S. Narayanan, D. Pinzaru, *Chem. Soc. Rev.* **2014**, *43*, 4714–4727. DOI: https://doi.org/10.1039/C4CS00020J.
- [4] J. E. Geusic, H. M. Marcos, L. G. Van Uitert, *Appl. Phys. Lett.* **1964**, *4*, 182–184. DOI: https://doi.org/10.1063/1.1753928.
- [5] M. Inoue, R. Fujikawa, A. Baryshev, A. Khanikaev, P. B. Lim, H. Uchida, O. Aktsipetrov, A. Fedyanin, T. Murzina, A. Granovsky, *J. Phys. D: Appl. Phys.* **2006**, *39*, R151. DOI: https://doi.org/10.1088/0022-3727/39/8/R01.
- [6] S. Geller, M. A. Gilleo, *Acta Crystallogr.* **1957**, *10*, 239. DOI: https://doi.org/10.1107/S0365110X57000729.
- [7] M. Valldor, A. Uthe, R. Rückamp, *Inorg. Chem.* **2011**, *50*, 10107–10112. DOI: https://doi.org/10.1021/ic201057h.
- [8] O. A. Petrenko, C. Ritter, M. Yethiraj, D. McK Paul, *Phys. Rev. Lett.* **1998**, *80*, 4570. DOI: https://doi.org/10.1103/PhysRevLett.80.4570.
- [9] T. Yavorskii, M. Enjalran, M. J. P. Gingras, *Phys. Rev. Lett.* **2006**, *97*, 267203. DOI: https://doi.org/10.1103/PhysRevLett.97.267203.
- [10] J. A. M. Paddison, H. Jacobsen, O. A. Petrenko, M. T. Fernández-Díaz, P. P. Deen, A. L. Goodwin, *Science* **2015**, *350*, 179–181. DOI: https://doi.org/10.1126/science.aaa5326.
- [11] A. P. Ramirez, *Annu. Rev. Mater. Sci.* **1994**, *24*, 453–480. DOI: https://doi.org/10.1146/annurev.ms.24.080194.002321.

- [12] R. Braun, S. Kemmler-Sack, *J. Solid State Chem.* **1986**, *64*, 76–80. DOI: [https://doi.org/10.1016/0022-4596\(86\)90123-4](https://doi.org/10.1016/0022-4596(86)90123-4).
- [13] M. B. Sanders, J. W. Krizan, R. J. Cava, *J. Mater. Chem. C* **2016**, *4*, 541–550. DOI: <https://doi.org/10.1039/C5TC03798K>.
- [14] SMART and SAINT, Area Detector Software Package and SAX Area Detector Integration Program; Bruker Analytical X-ray; Madison, WI, USA, **1997**.
- [15] SADABS, Area Detector Absorption Correction Program; Bruker Analytical X-ray; Madison, WI, USA, **1997**.
- [16] G. M. Sheldrick, *SHELXTL, version 5.1* **1997**, University of Göttingen: Göttingen Germany.
- [17] V. Petricek, M. Dusek, L. Palatinus, *Jana2006* **2006**, The crystallographic computing system; Institute of Physics: Praha, Czech Republic.
- [18] J. Rodriguez-Carvajal, *Physica B* **1993**, *192*, 55. DOI: [https://doi.org/10.1016/0921-4526\(93\)90108-l](https://doi.org/10.1016/0921-4526(93)90108-l).
- [19] W. A. Dollase, *J. Appl. Crystallogr.* **1986**, *19*, 267. DOI: <https://doi.org/10.1107/S0021889886089458>.
- [20] E. A. Davis, N. F. Mott, *Philos. Mag.* **1970**, *22*, 0903–0922. DOI: <https://doi.org/10.1080/14786437008221061>.
- [21] D. G. Barton, M. Shtein, R. D. Wilson, S. L. Soled, E. Iglesia, *J. Phys. Chem. B* **1999**, *103*, 630–640. DOI: <https://doi.org/10.1021/jp983555d>.
- [22] R. Ray, A. Himanshu, P. Sen, U. Kumar, M. Richter, T. Sinha, *J. Alloys Compd.* **2017**, *705*, 497–506. DOI: <https://doi.org/10.1016/j.jallcom.2017.02.080>.
- [23] J. P. Perdew, K. Burke, M. Ernzerhof, *Phys. Rev. Lett.* **1996**, *77*, 3865. DOI: <https://doi.org/10.1103/PhysRevLett.77.3865>.
- [24] K. Koepnik, H. Eschrig, *Phys. Rev. B* **1999**, *59*, 1743. DOI: <https://doi.org/10.1103/PhysRevB.59.1743>.
- [25] <https://www.fplo.de>.
- [26] Y. Takikawa, S. Ebisu, S. Nagata, *J. Phys. Chem. Solids* **2010**, *71*, 1592. DOI: <https://doi.org/10.1016/j.jpcs.2010.08.006>.
- [27] U. V. Valiev, J. B. Gruber, F. U. Dejun, V. O. Pelenovich, G. W. Burdick, M. E. Malysheva, *J. Rare Earths* **2011**, *29*, 776–782. DOI: [https://doi.org/10.1016/S1002-0721\(10\)60541-8](https://doi.org/10.1016/S1002-0721(10)60541-8).
- [28] H. Samata, N. Wada, T. C. Ozawa, *J. Rare Earths* **2015**, *33*, 177–181. DOI: [https://doi.org/10.1016/S1002-0721\(14\)60399-9](https://doi.org/10.1016/S1002-0721(14)60399-9).
- [29] S. Hatscher, H. Schilder, H. Lueken, W. Urland, *Pure Appl. Chem.* **2005** *77*, 497–511. DOI: <https://doi.org/10.1351/pac200577020497>.
- [30] C. Opagiste, C. Barbier, R. Haettel, R. M. Galéra, *J. Magn. Magn. Mater.* **2015**, *378*, 402–408 DOI: <https://doi.org/10.1016/j.jmmm.2014.11.070>.
- [31] D. L. Rosusseau, R. P. Bauman, S. P. S. Porto, *J. Raman Spectrosc.* **1981**, *10*, 253. DOI: <https://doi.org/10.1002/jrs.1250100152>.
- [32] E. Kroumova, M. I. Aroyo, J. M. Perez Mato, A. Kirov, C. Capillas, S. Ivantchev, H. Wondratschek, *Phase Transitions* **2003**, *76*, 155. DOI: <https://doi.org/10.1080/0141159031000076110>.
- [33] J. P. Hurrell, S. P. S. Porto, I. F. Chang, S. S. Mitra, R. P. Baum, *Phys. Rev.* **1968**, *173*, 851. DOI: <https://doi.org/10.1103/PhysRev.173.851>.
- [34] P. Grunberg, J. A. Koningstein, L. G. van Uitert, *J. Opt. Soc. Am.* **1971**, *61*, 1613. DOI: <https://doi.org/10.1364/JOSA.61.001613>.
- [35] J. J. Song, P. B. Klein, R. L. Wadsack, M. B. Selders, S. Mroczowski, R. K. Chang, *J. Opt. Soc. Am.* **1973**, *63*, 1135. DOI: <https://doi.org/10.1364/JOSA.63.001135>.
- [36] R.-L. Wadsack, J. L. Lewis, B. E. Argyle, R. K. Chang, *Phys. Rev. B* **1971**, *3*, 4243. DOI: <https://doi.org/10.1103/PhysRevB.3.4242>.
- [37] R. C. Middleton, D. V. S. Muthu, M. B. Kruger, *Solid State Commun.* **2008**, *148*, 310. DOI: <https://doi.org/10.1016/j.ssc.2008.09.002>.
- [38] K. Sawada, T. Nakamura, A. Adachi, *J. Appl. Phys.* **2016**, *120*, 143102. DOI: <https://doi.org/10.1063/1.4964444>.
- [39] C. L. Lin, Y. C. Li, X. D. Li, R. Li, J. F. Lin, J. Liu, *J. Appl. Phys.* **2013**, *114*, 163521. DOI: <https://doi.org/10.1063/1.4827836>.
- [40] C. Himcinschi, J. Rix, C. Röder, M. Rudolph, M.-M. Yang, D. Rafaja, J. Kortus, M. Alexe, *Sci. Rep.* **2019**, *9*, 379. DOI: <https://doi.org/10.1038/s41598-018-36462-5>.
- [41] K. Binnemans, *Coord. Chem. Rev.* **2015**, *295*, 1–45. DOI: <https://doi.org/10.1016/j.ccr.2015.02.015>.
- [42] J. B. Gruber, U. V. Valiev, G. W. Burdick, S. A. Rakhimov, M. Pokhrel, D. K. Sardar, *J. Lumin.* **2011**, *131*, 1945. DOI: <https://doi.org/10.1016/j.jlumin.2011.03.057>.
- [43] R. Praveena, V. Venkatramu, P. Babu, C. K. Jayasankar, T. Troster, W. Sievers, G. Wortmann, *J. Phys. : Conf. Ser.* **2008**, *121*, 042015. DOI: <https://doi.org/10.1088/1742-6596/121/4/042015>.
- [44] Q. G. Zeng, Z. J. Ding, Z. M. Zhang, Y. Q. Sheng, *J. Phys. Chem. C* **2010**, *114*, 4895. DOI: <https://doi.org/10.1021/jp911791u>.

Received: March 17, 2020